VOLUMETRIC 3D PRINTING OF ELASTOMERS BY TOMOGRAPHIC BACK-PROJECTION

A PREPRINT

Damien Loterie*
Laboratory of Applied Photonics Devices
Ecole Polytechnique Fédérale de Lausanne
Lausanne, CH-1015, Switzerland
damien.loterie@epfl.ch

Paul Delrot*
Laboratory of Applied Photonics Devices
Ecole Polytechnique Fédérale de Lausanne
Lausanne, CH-1015, Switzerland
paul.delrot@epfl.ch

Christophe Moser
Laboratory of Applied Photonics Devices
Ecole Polytechnique Fédérale de Lausanne
Lausanne, CH-1015, Switzerland
christophe.moser@epfl.ch

November 8, 2018

ABSTRACT

Most additive manufacturing methods such as fused-deposition modelling, selective laser melting or stereolithography create objects sequentially one layer at a time. This type of process imposes limitations on the shapes and the materials that can be printed. For example, overhanging structures need additional supports during printing, and soft or elastic materials are difficult to print since they deform as new layers are added. While casting can be used instead to create certain elastic parts, design freedom is limited because cavities or tubes are difficult to unmold. Here we use a volumetric 3D printing method based on tomography, where the entire volume of a photopolymerizable resin is solidified at the same time. We demonstrate very rapid (<30s) printing of a variety of complex structures with acrylates and silicones.

***K*eywords** 3D printing · additive manufacturing · elastomer · tomography

1 Introduction

Patient-tailored soft medical devices such as tissue-like surgical models and rubber-like hearing aids are currently produced through casting or additive manufacturing [1, 2]. However, each of these manufacturing techniques suffers from specific limitations that affect both the process chain and patient care.

In casting, a part is created by pouring a liquid material into a solid mold. The poured material then solidifies through thermal, chemical or optical treatment, and the part is unmolded. Though casting allows producing elastomeric parts, it has a limited design freedom as undercuts and tubes are difficult to mold [3, 4, 5]. Casting a tubular part requires using a solid conduit to facilitate unmolding (see Fig. 1a). Hence, complex hollow parts that are essential for medical applications, for instance to create vasculatures models for the education of surgeons (see Fig. 1b) or to make vents in hearing aids [6], are challenging to cast [7].

On the other hand, the layer-by-layer fabrication process of additive manufacturing techniques offers more design freedom than casting [1, 2, 3, 5, 8, 9]. Stereolithography (see Fig. 1c) is currently the additive manufacturing technique of choice for producing hearing aid shells and surgical guides [10, 11]. In this technique, a part is built by sequentially

*These authors contributed equally to the present work

solidifying cross-sections of a liquid resin with UV light patterns (see Fig. 1c). The build platform is lifted between each exposure step to replenish the layer of liquid resin beneath the part being produced [12].

When producing complex parts with stereolithography, solid support struts must be fabricated together with the part to hold the overhanging pieces of the structure (see Fig. 1c) [13]. Hence, significant manual post-processing of the parts is needed to remove these solid support struts [7], which results in long lead times that can be detrimental to patient care.

In addition, the motion of the build platform requires using low viscosity liquid resins (<4 Pa s) [3, 12, 14, 15]. Thus, existing stereolithographic devices cannot print elastomeric materials relevant for biomedical applications, such as high-shore silicone (> 5 Pa s viscosity), which is highly demanded because of its biocompatibility, durability and compliance.

Here, we use a tomographic volumetric printing method [16], analogous to a recently proposed method at UC Berkeley [17], to overcome the limitations of both casting and additive manufacturing techniques for the production of patient-tailored soft medical devices.

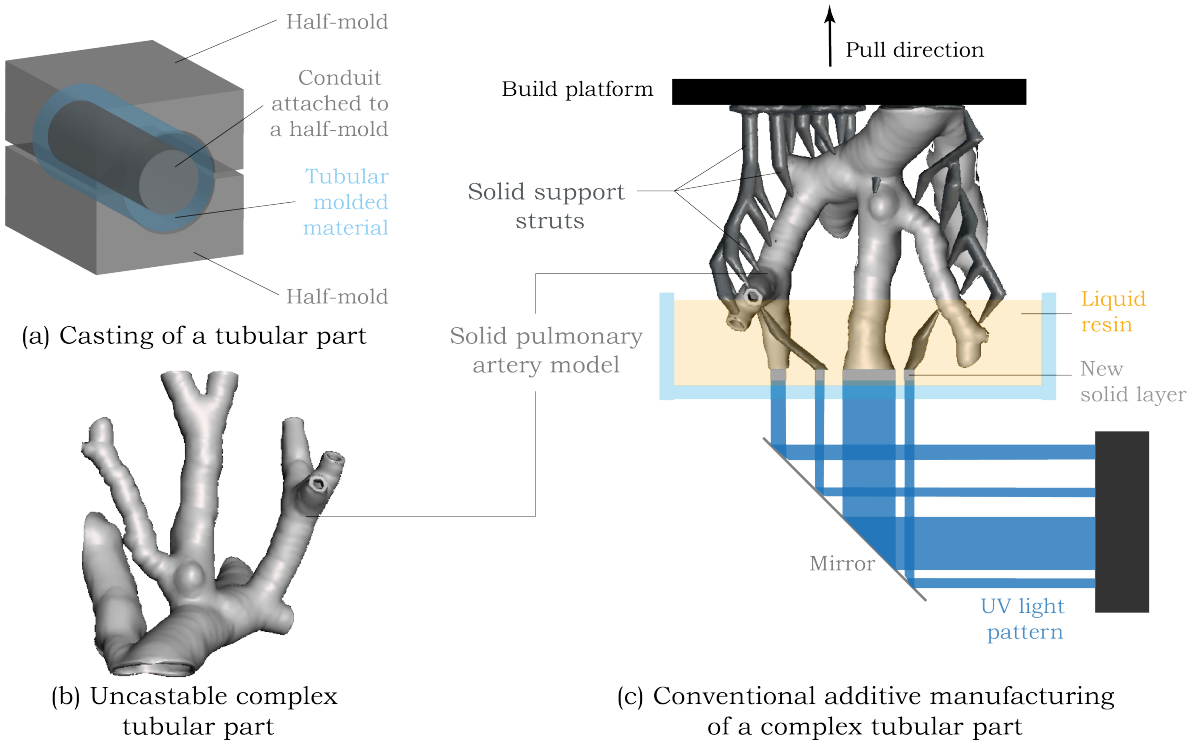

Figure 1: Limitations of conventional casting and additive manufacturing.

2 Materials and methods

2.1 Tomographic volumetric 3D printing

Tomographic 3D printing is inspired by computed tomography (CT) scans in biomedical imaging. In computed tomography, a series of X-ray radiographs of a patient or object are acquired from different angles. These radiographic projections are then processed with a tomographic algorithm in order to reconstruct cross-sectional images of the scanned object. The cross-sectional images represent the distribution of absorbed X-ray dose inside the object.

The mathematical theory at the foundation of this method is the Radon transform, which relates the projections at different angles with the cross-sectional images of the object. The corresponding inverse Radon transform allows retrieving the cross-sections back from the projections. Over the years, a variety of more advanced tomography algorithms have been developed to also address issues such as noise, artefacts, different detector geometries, computation speed, etc. [18].

In tomographic 3D printing, the principle of CT scans is used in reverse. First, a digital model of the desired object is loaded. Based on this model, cross-sectional images of the object are generated (voxelization). Then, projections from a set of many angles from 0 to 360° are calculated using the Radon algorithm (or any other tomography algorithm) such that when all these projections are displayed into a homogeneous volume of absorbing material, the cumulative absorbed dose distribution due to the projections reproduces the shape of the three-dimensional object inside the material. If a liquid photopolymer is used as a target material and visible light is used for the projections, locations inside the photopolymer where a high dose of light was applied will solidify whereas other locations remain below the solidification threshold [19] (see Fig. 2(a)).

In other words, this process creates a solid object of the desired shape inside the volume of photopolymer (see Fig. 2(b)). An example of an object and its projections is shown in Fig. 2(c) and 2(d).

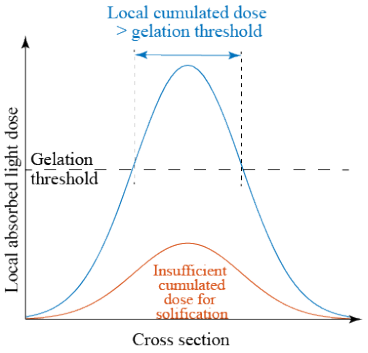

(a) The gelation threshold allows to solidify a local polymer volume through cumulative irradiation

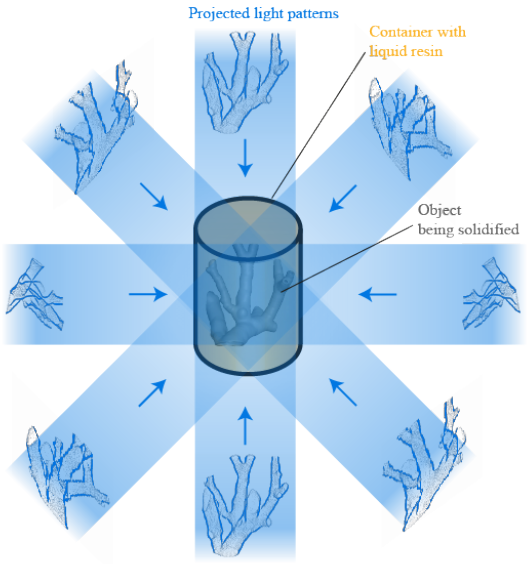

(b) Concept of volumetric additive manufacturing

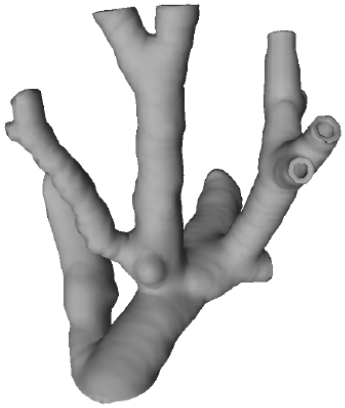

(c) 3D model of pulmonary artery

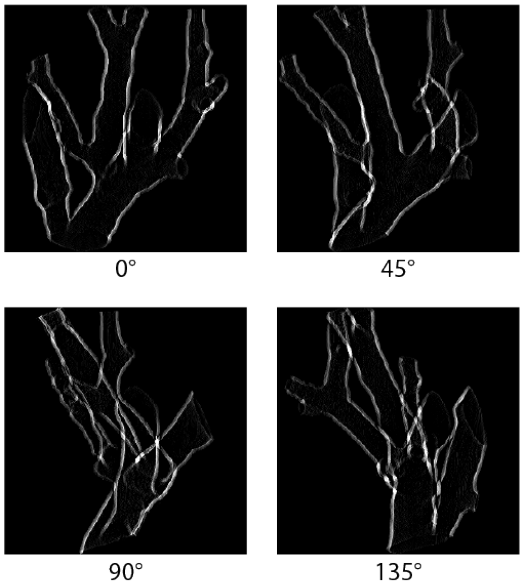

(d) filtered backprojections as applied to the resin

Figure 2: Physical basis of the tomographic volumetric printing approach. The liquid resin (yellow cylinder in b) is illuminated from various directions using suitable light patterns (blue). This deposits a controllable cumulated dose in specific locations inside the resin, thereby creating the three-dimensional object. Here, the object is a pulmonary artery model (c). A sample of projections used to fabricate this object is shown in (d).

2.2 Positive thresholding

To calculate a set of projections whose cumulative sum is exactly equal to the desired dose distribution, it is necessary to apply a Ram-Lak filter (also called ramp filter) to the Radon projections, yielding so-called "filtered back-projections". The filter compensates for the inherent blurring effect due to the projections [18].

However, it causes negative values to appear in the filtered back-projections, which cannot physically be applied to the target volume. A straightforward solution to this problem is to discard the negative values and illuminate the material with only the positive part of the patterns. This approximation works successfully in many cases, although it can cause some artefacts to appear on the printed object, such as a rounding effect on sharp corners (see Fig. 3).

To mitigate this, an optimization algorithm can be used to find the best possible projections under the constraint of positivity [17, 20]. Another solution could be to use a material that is sensitive to two different wavelengths of light, one to initiate the reaction (positive values) and one to inhibit or revert it (negative values).

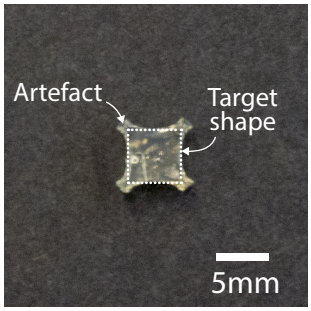

Figure 3: Artefacts due to positive threshold (top-view of printed cube)

2.3 Optical setup

Our optical setup is shown in Fig. 4. Six 405nm laser diodes, with a combined nominal power of 6.4W, are collimated and combined into a single beam with closely spaced mirrors. The combined beam is then coupled into a square-core optical fiber (CeramOptec WF 70x70/115/200/400N, core size 70μm by 70μm, numerical aperture 0.22), which allows homogenizing the beam from the laser diodes and matching to the rectangular aperture of the modulator for increasing the light efficiency. The output of the fiber is then magnified and projected onto a digital micromirror device (DMD) via an aspheric lens and a set of orthogonal cylindrical lenses. The cylindrical lenses have different focal lengths, which allows adjusting the square beam from the fiber to the rectangular area of the DMD.

The DMD suffers from diffractive effects due to the blazed grating formed by the individual micromirrors when they are in their tilted state. This effect can cause a large fraction of the reflected light to be lost in diffracted orders depending on the incidence angle of the illumination beam. To optimize the reflected efficiency, the DMD in our setup is fixed on a rotational mount in such a way that the rotation axis of the device corresponds to the diagonal tilt axis of the micromirrors. Then, we simply rotated the DMD until the power in the main reflected order was maximized. The rotation angle was approximately 7° in our case, but in general it depends on the precise wavelength of the laser, the pixel pitch of the DMD and the tilt angle of the micromirrors.

The surface of the DMD is imaged via a 4f-system into a cylindrical glass vial containing the photopolymer. In the Fourier plane, an aperture blocks the unwanted diffraction orders from the DMD. A concave cylindrical lens placed in close proximity to the vial corrects the distortion caused by the cylindrical interface of the vial. In this setup, the addressable volume inside the photopolymer is approximately 17.5mm x 17.5mm x 23mm. When all the DMD pixels are in their 'ON' state, the power of the light beam sent into the vial is approximately 1.6W.

2.4 Etendue and resolution

Most tomography algorithms assume a perfectly straight beam of light, but in practice every light beam has a certain divergence, as illustrated in Fig. 5. This is one of the factors that limits the resolution with which a three-dimensional dose distribution can be created inside the photosensitive material. Assume that the build volume has a diameter L_B and that the voxel size (size length) in the center of the build area is L_{vox}. The size L_{vox} corresponds to the pixel size of the DMD after being imaged into the build volume, i.e. after magnification or demagnification.

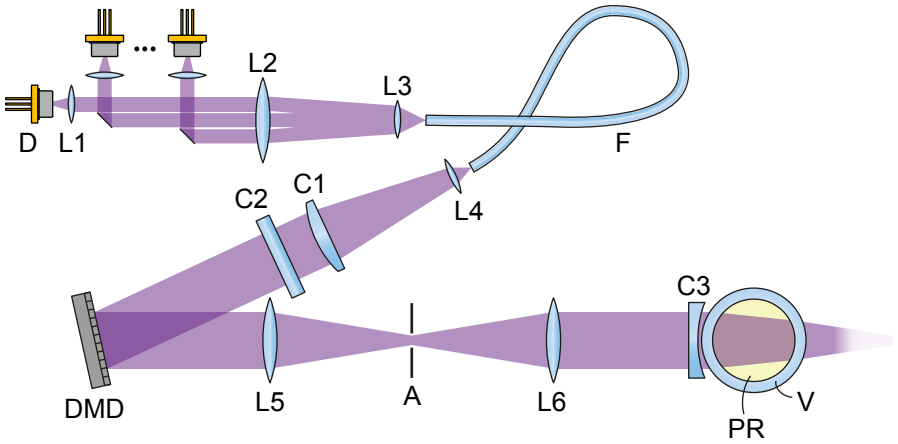

Figure 4: Experimental setup. D: 405nm laser diode; L1: f = 3.1mm aspheric lens ; L2: f = 200mm lens; L3: 3.1mm aspheric lens; F: 70μm by 70μm square-core optical fiber; L4:f = 3mm aspheric lens; C1: f = 250mm cylindrical lens; C2 : f = 300mm cylindrical lens; DMD: digital micromirror device (Vialux V-7000 VIS); L5: f = 150mm lens; A: variable aperture; L6: f = 250 mm lens; C3: f = -30mm concave cylindrical lens; V: cylindrical vial (glass, outer diameter 34mm, wall thickness 1mm); PR: photopolymer.

Assume further that the goal is to limit the divergence such the light beam illuminating this voxel grows to at most $(1+p)\cdot L_{vox}$ at the edge of the build volume. In that case, the divergence angle should be at most $tan\theta = pL_{vox}/L_B$ and the numerical aperture of this beam should be below $NA = nsin\theta \sim npL_{vox}/L_B$, where n is the index of the resin. This in turn has implications on the étendue of the light source illuminates the DMD. If the light source provides light for all of the voxels spanning the build volume (i.e. a number $N = L_B/L_{vox}$ of voxels), and each voxel has a side-length and NA as calculated above, then the light source should have an étendue of $L_S NA_S = npL_{vox}$, where L_S is the width and NA_S the numerical aperture of the light source.

In our case, with a $L_S = 70\mu m$ square core fiber, $NA_S = 0.22$, a refractive index of 1.47 and a DMD pixel size of 23μm after magnification, the divergence of the light beam causes a maximum spread of approximately $p = 46\%$. This means the optical resolution is approximately 23μm in the center of the build volume and 33μm on the edge. As explained later, other effects such as scattering and chemical diffusion of the polymerization reaction can further limit the achievable resolution.

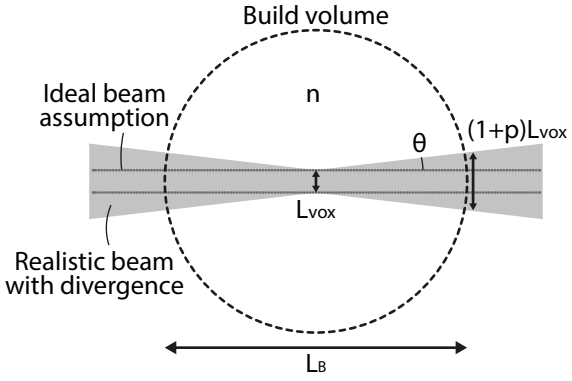

Figure 5: Divergence of the light inside the build volume.

2.5 Resin formulations

The resin formulations used in this study are described in Table 1. The di-pentaerythritol pentaacrylate and aliphatic urethane diacrylate were gently provided by Sartomer.

Table 1: Resin formulations

Name	Description	Amount	Composition	Viscosity (Pa.s)
A	Acrylate	100 wt.%	Di-pentaerythritol pentaacrylate (SR399; Sartomer, France)	10.6 (25°C)
		0.6 mol.m^{-3}	Phenylbis(2,4,6-trimethylbenzoyl)phosphine oxide (97%; Sigma Aldrich, USA)	
U	Urethane	100 wt.%	Aliphatic urethane diacrylate (CN9012; Sartomer, France)	9-15 (50°C)
		0.6 mol.m^{-3}	Phenylbis(2,4,6-trimethylbenzoyl)phosphine oxide (97%; Sigma Aldrich, USA)	
S	Silicone	93 wt.%	Vinyl-terminated PDMS 62 kg/mol (DMS-V41; Gelest, USA)	10 (25°C)
		4.7 wt.%	Fumed silica reinforced vinyl-terminated PDMS 28 kg/mol (DMS-V31S15; Gelest, USA)	3 (25°C)
		2.3 wt.%	(Mercaptopropyl)Methylsiloxane - dimethylsiloxane 3.6 kg/nol (GPC-367; Genesee Polymer Co., USA)	0.15 (25°C)
		2.25 mol.m^{-3}	Ethyl (2,4,6-trimethylbenzoyl)phenylphosphinate (TPO-L, 95%; Fluorochem, UK)	

The resins A and U (see Table 1) were prepared by magnetically stirring at 500 rpm the compounds in glass jars heated at 100°C for 1h . To remove bubbles trapped in the resins A and U, the vials were also centrifuged at 500 rpm for 30 seconds prior to use. The resin S was prepared by hand-mixing the compounds and degassing the end-mixture at -12 psi for 20 min in order to prevent polymerization inhibition of silicone by oxygen.

The materials' tensile properties were measured on a universal testing machine (Zwick/Roell Z010) according to ASTM D638 standard.

Our volumetric additive manufacturing technique sets some requirements on the printable resins, notably on their viscosity, transparency and scattering properties. We discuss these requirements in section 3.2.

3 Results and Discussion

3.1 Printing process

The printing process is better understood with the supplementary video. Fig. 6(a) shows the printing result after the post-processing steps.

For the resins A and U, the post-processing was achieved by filtering the content of the photopolymer vial to both collect the printed part and to recycle the unpolymerised ink content. The part was further cleaned for 30 seconds in an ultrasonic bath of isopropyl alcohol, followed by a drying step of 10 minutes and a post-curing step of 3 min at 150 mW/cm^2 with a 405-nm LED light source.

As shown in Fig. 6(a), the volumetric 3D printing process allows to produce parts with an overall good quality, which we further analyse on a complex hollow part in section 3.2.

3.2 Printing accuracy

Figs. 6(b-c) show the accuracy of an acrylate printed part with respect to the 3D digital model. We observe that the printing accuracy is fair on the overall length, height and width of the part (-11 % to +10%) whereas the deviation to the model is larger on the diameter of the different holes and tubes (-50% to +10%). However, this hearing aid part demonstrates the ability of the volumetric technique to print complex parts with tubes and canals.

This printing accuracy as well as the printing resolution depends on both the optical and chemical phenomena at play in volumetric additive manufacturing.

Besides the etendue of the illumination source (see section 2.4), other optical parameters affect the printing resolution. First, the light dose deposited in the photopolymer is here computed through a tomographic reconstruction algorithm, followed by a positive thresholding step (see section 2.2 for further details). Though the positive thresholding

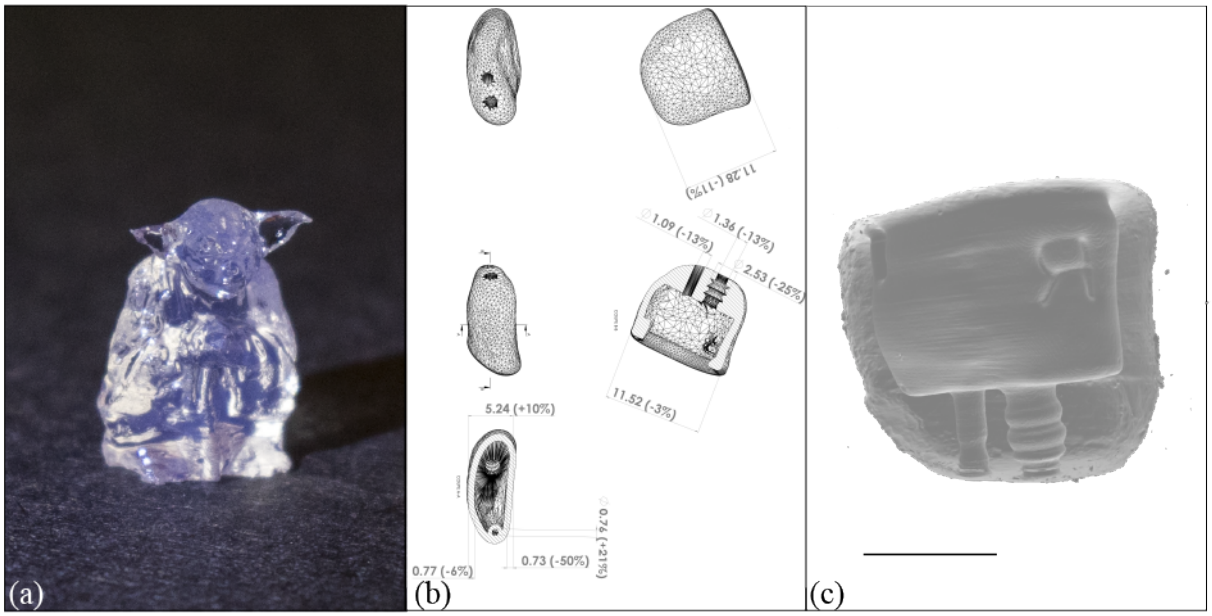

Figure 6: (a) Post-processed result of the printing visible on the supplementary video (b) MicroCT measurement of the printing accuracy with respect to the digital model of a complex hearing aid part, all dimensions are in mm. Resin A was used. (c) 3D rendering of the printed and MicroCT measured hearing aid part of Fig. 6(b), scale bar: 5 mm.

accounts for the physical impossibility to deliver negative light dose values, it degrades the quality of the tomographic reconstruction, especially on the printed object's edges. Previous work showed that the computed light 2D patterns could be optimized using a double thresholding convergence algorithm [17], which we will include in our future work.

3.2.1 Two-color scheme

Delivering negative light dose values could be achieved by using a two-color single photo-initiation and photo-inhibition system as recently demonstrated for sub-diffraction lithography [21]. In this system, a photo-inhibiting species (tetraethylthiuram disulfide) sensitive to UV-light is orthogonally combined with a blue-light sensitive photoinitiator (camphorquinone). However, implementing this two-color scheme for tomographic volumetric additive manufacturing would first require to thoroughly investigate the kinetics find a photo-inhibitor that is both suitable for acrylate formulations and can quickly recombine. Another two-color scheme would consist in engineering a photoinitiator that creates free-radicals only when irradiated by both wavelengths.

3.2.2 Centrifugal acceleration and sedimentation

The effect of the centrifugal acceleration on the resolution of the volumetrically printed parts can be neglected compared to the gravitational acceleration since the rotation speed of our process (12-20 rpm) induces at most a $4{\cdot}10^{-2}g$ acceleration for the sections of the object located 1 cm away from the rotation axis.

However, the sedimentation of sections of the objects during the 15 to 40 seconds printing time sets specifications on the resins' dynamic viscosity. The sedimentation speed v for an object section L whose cured density is ρ_{solid} into a photopolymer of density ρ_{liquid} and dynamic viscosity η can be written in a gravitational acceleration g as [22]:

$$v = \frac{(\rho_{solid} - \rho_{liquid})gL^2}{18\eta} \tag{1}$$

Let us assume that an object is cured from a raw monomer resin to a full polymer, for instance from methyl methacrylate (ρ_{liquid} = 940 kg/m^3) to poly-methyl methacrylate (ρ_{solid} = 1180 kg/m^3) in 15 seconds. Limiting the sedimentation depth, and thus the vertical resolution, to 50 μm for an object section of L=2 mm would require to use a resin with a dynamic viscosity η larger than 150 Pa s. As pure methyl methacrylate has a viscosity of $\eta_{MMA} = 0.6 \cdot 10^{-3}$Pa s, it is not suited for volumetric printing.

Practically since our resins are made of prepolymer and not raw monomer as in the example above, the density difference between the liquid and solid resin states is thus lower than in the previous example, which allows for curing time in the 30-second range without significant detrimental effect on the printing quality. Furthermore, our printing system does not induce any mechanical motion within the build volume, which allows for using high-viscosity resins (see Table 1) that are less prone to sedimentation issues (see Eq. 1). Interestingly, such viscous resins would be challenging to print with existing layer-by-layer systems because of the motion of the build platform [3, 12, 14, 15].

One will also notice that using highly-viscous resins also reduces the diffusion of free-radicals during the printing process and therefore reduces proximity effect [19].

3.2.3 Resin optical properties

Finally, the volumetric additive manufacturing method described in the present work sets some requirements on the optical properties of the resins.

First, the tomographic volumetric printing method requires that the light patterns propagates through the whole diameter of the build volume (see section 2.2). Hence, knowing the absorption coefficient α of the photoinitiator for the illumination wavelength, we adjusted the photoinitiator concentration c so that the optical attenuation length l is longer than the width of the printed objects:

$$c = \frac{1}{\alpha l} \tag{2}$$

We hypothesize that this will ultimately limit the size of the object printable with tomographic volumetric printing as the low photoinitiator amount required for large objects will result in a poor polymer conversion and poor mechanical properties of the printed parts. Higher photoinitiator amounts than that defined by Eq. 2 could be used provided that a correction for the exponential decay of light intensity is included in the tomographic reconstruction algorithm.

In other words, suitable resins for volumetric additive manufacturing should have a strong reactivity and low absorption, which is to be compared to the requirements for layer-by-layer printers where both a strong reactivity and strong absorption of resins is needed to obtain well-defined layers [23].

3.3 Hollow solid and elastomeric structures

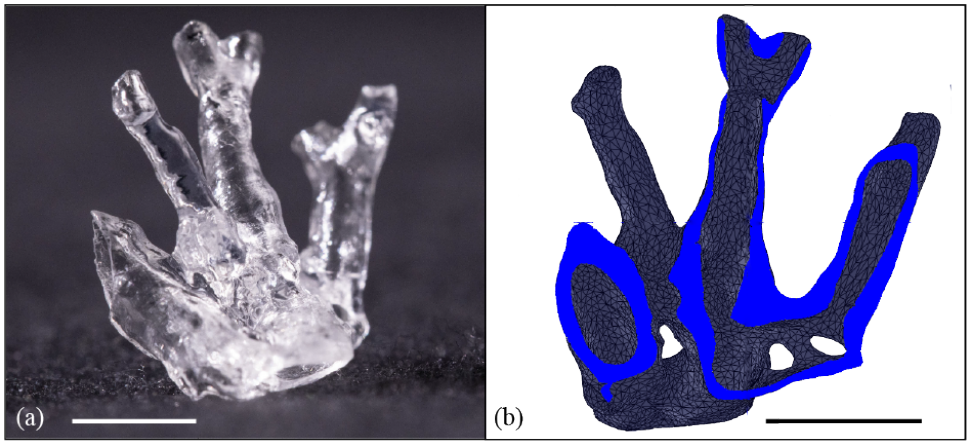

Figure 7: (a) Mouse pulmonary artery model printed with the method of the present work in 32.5s based on the model of Fig. 2 with the resin A. Scale bar: 5 mm (b) Cross-section view of the Micro-CT scanned printed part showed in Fig. 7. The blue color shows solid walls.

Fig. 7(a) shows that complex hollow structures, challenging to produce with existing manufacturing techniques, can be quickly printed without any support struts.

The printed pulmonary model was further scanned with a Micro-CT (Skyscan 1076, 9 , Bruker) at a resolution of 9-μm resolution to reveal the small arteries printed, with a smallest achieved diameter of 1.4 mm (see Fig. 7(b)).

Tomographic volumetric printing allows using highly-viscous resins with a wide range of mechanical properties as shown in Fig. 8(a). The tensile properties of the printable materials spans from plastic (see red curve in Fig. 8(a)) to elastomeric with modulus from 356 MPa to 280 kPa (see blue and yellow curves in Fig. 8(b)).

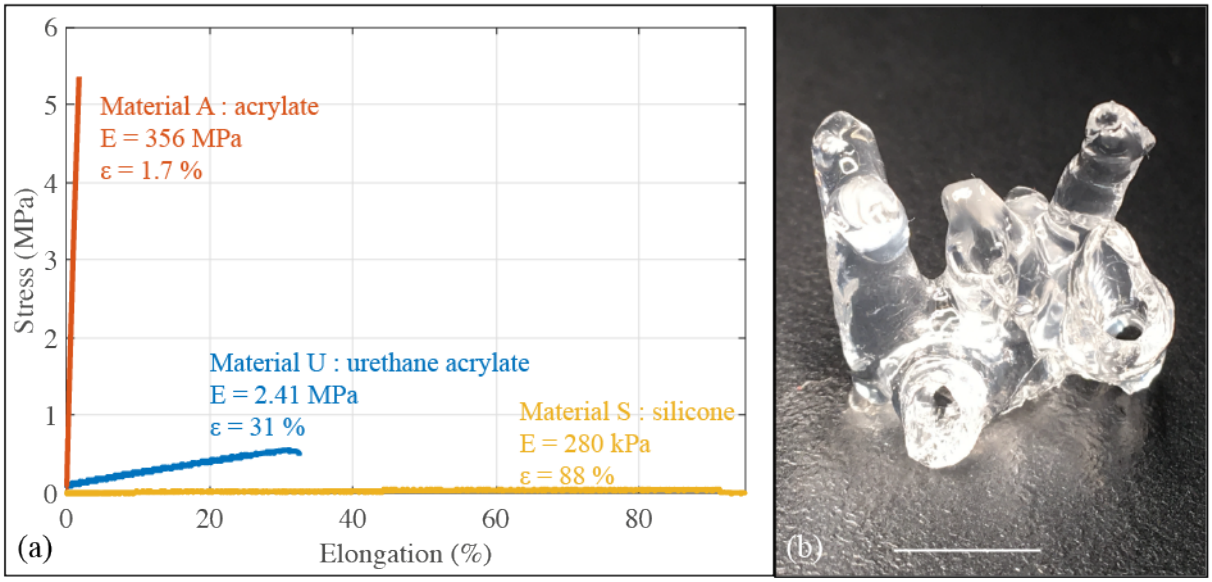

Figure 8: (a) Tensile test to failure of some the materials printed with tomographic volumetric printing (see Table 1), E stands for elastic modulus and ϵ for elongation at break. (b) Mouse pulmonary artery model volumetrically printed in 15 seconds with the silicone resin S (see Table 1). Scale bar: 5 mm.

More specifically, to produce surgical models that mimic the mechanical properties of biological tissues, we developed thiol-ene silicone resins with low elastic moduli (E = 280 kPa for instance for the resin S). The developed silicone resin complies with the viscosity and optical requirements defined in section 3.2. The scattering properties of the resin S were challenging to optimize since we experimentally observed that mixtures with thiol crosslinkers having functionality larger than about 4 to 6 will yield turbid resins, not suited for tomographic volumetric printing.

Using the silicone resin S, we were able to print the mouse pulmonary model of Fig. 2. Though the printed structure is extremely soft, channels as small as 1.8 mm were successfully printed as shown in Fig. 8(b). As the printed structure was extremely tacky, the post-processing steps included a post-curing of the silicone part in a mixture of thiol crosslinker and photo-initiatior (TPO-L) for 5 min at 100 mW/cm^2. This post-processing step successfully reduced the object tackiness.

4 Conclusion

We demonstrated additive manufacturing of complex objects on the scale of 2 cm, such as a hearing aid shell and a miniature model of a pulmonary artery. We use a volumetric approach based on tomography, which is very fast compared to layer-by-layer additive manufacturing as we are able to print parts in less than 30s. Because the method does not require motion of the object with relative to the resin during printing, viscous resin formulations can be used. In addition to acrylate-based resins, we demonstrate that a silicone-based resin can be used to produce complex vasculature patterns. We expect that this method will enable the fabrication of soft and elastomeric parts that were not accessible by other methods such as casting or layer-by-layer additive manufacturing, enabling a range of new applications for example in surgical planning.

Acknowledgments

D.L. and P.D. acknowledge support from EPFL-Innogrant and EPFL-Enable for the *Tomoprint* project. The authors would like to thank Yasmine Meharzi Boulanaache (LBO-EPFL) for helpful discussions on Micro-CT measurements.

Supplementary video

`https://youtu.be/31xHZvUP1Ls`

References

[1] Ian Gibson, David Rosen, and Brent Stucker. *Additive manufacturing technologies: 3D printing, rapid prototyping, and direct digital manufacturing, second edition*. Springer New York, New York, NY, January 2015.

[2] Manuel Schaffner, Jakob A Faber, Lucas Pianegonda, Patrick A Rühs, Fergal Coulter, and André R Studart. 3D printing of robotic soft actuators with programmable bioinspired architectures. *Nature Communications*, 9(1):878, February 2018.

[3] T J Wallin, J H Pikul, S Bodkhe, B N Peele, B C Mac Murray, D Therriault, B W McEnerney, R P Dillon, E P Giannelis, and R F Shepherd. Click chemistry stereolithography for soft robots that self-heal. *Journal of Materials Chemistry B*, 5(31):6249–6255, January 2017.

[4] Panagiotis Polygerinos, Nikolaus Correll, Stephen A Morin, Bobak Mosadegh, Cagdas D Onal, Kirstin Petersen, Matteo Cianchetti, Michael T Tolley, and Robert F Shepherd. Soft Robotics: Review of Fluid-Driven Intrinsically Soft Devices; Manufacturing, Sensing, Control, and Applications in Human-Robot Interaction. *Advanced Engineering Materials*, 19(12), December 2017.

[5] Nirveek Bhattacharjee, Cesar Parra-Cabrera, Yong Tae Kim, Alexandra P Kuo, and Albert Folch. Desktop-Stereolithography 3D-Printing of a Poly(dimethylsiloxane)-Based Material with Sylgard-184 Properties. *Adv. Mater. Weinheim*, page e1800001, April 2018.

[6] J Giannatsis and V Dedoussis. Additive fabrication technologies applied to medicine and health care: A review. *International Journal of Advanced Manufacturing Technology*, 40(1-2):116–127, January 2009.

[7] Formlabs. Custom Silicone Ear Molds with the Form 2. Technical report, March 2018.

[8] Jian Sun and Fu-Qiang Zhang. The Application of Rapid Prototyping in Prosthodontics. *Journal of Prosthodontics*, 21(8):641–644, July 2012.

[9] Justin Poelma and Jason Rolland. Rethinking digital manufacturing with polymers. *Science*, 358(6):1384–1385, December 2017.

[10] Christian G Sandström. The non-disruptive emergence of an ecosystem for 3D Printing — Insights from the hearing aid industry's transition 1989–2008. *Technological Forecasting and Social Change*, 102:160–168, January 2016.

[11] Frederik Gelaude and Tim Clijmans. Customized surgical guides, methods for manufacturing and uses thereof. US Patent Office, November 2017.

[12] John R Tumbleston, David Shirvanyants, Nikita Ermoshkin, Rima Janusziewicz, Ashley R Johnson, David Kelly, Kai Chen, Robert Pinschmidt, Jason P Rolland, Alexander Ermoshkin, Edward T Samulski, and Joseph M DeSimone. Additive manufacturing. Continuous liquid interface production of 3D objects. *Science*, 347(6228): 1349–1352, March 2015.

[13] Paulo Jorge Bártolo. *Stereolithography*. Materials, Processes and Applications. Springer Science & Business Media, March 2011.

[14] Samuel Clark Ligon, Robert Liska, Jürgen Stampfl, Matthias Gurr, and Rolf Mülhaupt. Polymers for 3D Printing and Customized Additive Manufacturing. *Chem. Rev.*, 117(15):10212–10290, August 2017.

[15] Carl J Thrasher, Johanna J Schwartz, and Andrew J Boydston. Modular Elastomer Photoresins for Digital Light Processing Additive Manufacturing. *ACS Appl. Mater. Interfaces*, 9(45):39708–39716, November 2017.

[16] Damien Loterie, Paul Delrot, and Christophe Moser. Method and apparatus for three-dimensional fabrication by tomographic back projections, August 2018.

[17] Brett Kelly, Indrasen Bhattacharya, Maxim Shusteff, Robert M Panas, Hayden K Taylor, and Christopher M Spadaccini. Computed Axial Lithography (CAL): Toward Single Step 3D Printing of Arbitrary Geometries. *arXiv*, page arXiv:1705.05893, May 2017.

[18] Aninash C Kak and Malcolm Slaney. *Principles of Computerized Tomographic Imaging*. SIAM, January 2001.

[19] Paul Delrot, Damien Loterie, Demetri Psaltis, and Christophe Moser. Single-photon three-dimensional microfabrication through a multimode optical fiber. *Opt. Express*, 26(2):1766–1778, January 2018.

[20] Yair Censor and Jan Unkelbach. From analytic inversion to contemporary IMRT optimization: Radiation therapy planning revisited from a mathematical perspective. *Physica Medica*, 28(2):109–118, April 2012.

[21] Timothy F Scott, Benjamin A Kowalski, Amy C Sullivan, Christopher N Bowman, and Robert R McLeod. Two-color single-photon photoinitiation and photoinhibition for subdiffraction photolithography. *Science*, 324 (5929):913–917, May 2009.

[22] Alexander Ya Malkin and Avraam I Isayev. *Rheology: Concepts, methods, and applications: Second edition*. Elsevier, A.V.Topchiev Institute of Petrochemical Synthesis, RAS, Moscow, Russian Federation, January 2011.

[23] Tommaso Baldacchini. *Three-Dimensional Microfabrication Using Two-Photon Polymerization*. Fundamentals, Technology, and Applications. William Andrew, September 2015.